

PCCP

Accepted Manuscript



This is an *Accepted Manuscript*, which has been through the Royal Society of Chemistry peer review process and has been accepted for publication.

Accepted Manuscripts are published online shortly after acceptance, before technical editing, formatting and proof reading. Using this free service, authors can make their results available to the community, in citable form, before we publish the edited article. We will replace this *Accepted Manuscript* with the edited and formatted *Advance Article* as soon as it is available.

You can find more information about *Accepted Manuscripts* in the [Information for Authors](#).

Please note that technical editing may introduce minor changes to the text and/or graphics, which may alter content. The journal's standard [Terms & Conditions](#) and the [Ethical guidelines](#) still apply. In no event shall the Royal Society of Chemistry be held responsible for any errors or omissions in this *Accepted Manuscript* or any consequences arising from the use of any information it contains.

Kinetic Monte Carlo simulation of the photodegradation process of polyester-urethane coatings

Koen N.S. Adema ^{a, b}, Hesam Makki ^{a, b}, Elias A.J.F. Peters ^a, Jozua Laven ^a, Leendert G.J. van der Ven ^a, Rolf A.T.M. van Benthem ^a, Gijsbertus de With^{*, a}

^a Eindhoven University of Technology, Laboratory of Materials and Interface Chemistry, Department of Chemical Engineering and Chemistry, P.O. Box 513, 5600 MB Eindhoven, The Netherlands

^b Dutch Polymer Institute (DPI), P.O. Box 902, 5600 AX Eindhoven, The Netherlands

* Corresponding author: G.deWith@tue.nl

Keywords:

Kinetic Monte Carlo; Simulation; Photodegradation; Polymer coating; Polyester-urethane.

Abstract

A numerical method to simulate reactions in a cross-linked polymer is developed and applied to the photodegradation process of polyester-urethane clearcoats during artificial exposure in a Weather-Ometer. This coarse-grained simulation method, which is based on a kinetic Monte Carlo scheme, is verified with experimental data on the depth-resolved changes in optical properties and chemical composition that have been previously determined. By modelling the depth-dependency of physical processes that occur in the coating, such as the absorption of photons and the diffusion of oxygen, the experimentally observed evolution of depth gradients in chemical composition can be well described by the simulation. A sensitivity analysis of individual simulation input parameters with respect to a set of resulting observables is performed and the results provide insight into the influence of specific reaction mechanisms on the overall degradation process and help to distinguish essential from less important processes. The values of input parameters that result in the most accurate simulation of the experimental data are determined with an optimisation procedure. In this way, the numerical values of several kinetic and physical parameters that are difficult to determine directly in an experimental way, such as various reaction rate constants, can be obtained from the simulations.

1 Introduction

Polymer coatings can serve a wide range of purposes, but their decorative and protective functions are still the most essential requirements for many industrial applications. The protective function is especially critical for a clearcoat that has to protect the underlying components of a typical multi-layered decorative coating from its environment. For outdoor coating applications, such as in the automotive or aerospace industry, this clearcoat has to resist severe stresses in terms of UV-radiation combined with temperature, humidity, (atmospheric) precipitation and mechanical wear^{1,2}. Stability against weathering is prerequisite for a clearcoat that is intended for exterior usage.

The majority of studies in the field of polymer weathering is based on experimental approaches. During the last years, however, the number of researchers who chose to follow simulation-based routes has increased. Initially, computer simulations in the field of polymer weathering were based on probabilistic approaches, in which the time evolution of the degrading system from its initial state to a degraded state may follow different possible pathways. An early, but very illustrative example of such a probabilistic approach is the work by Martin³. Subsequent research has mainly dealt with the evolution of surface topography during weathering, including the influence of pigments⁴ and the study on how (initial) degradation can influence further degradation⁵. The evolution of the surface topography is often related to the change in gloss due to a changing roughness, but relations with other coating properties (fracture toughness, reflectance, contact angle, yellowing, dielectric response) have been established as well⁵⁻⁷. Deterministic approaches to weathering simulations have also been explored, often based on so-called mechanistic models⁸, that is, mathematical descriptions of chemical and physical phenomena that take place during photodegradation. A mechanistic approach towards “time-to-failure” models, which are used to generate distribution functions of a coating’s lifetime, has been established by Bauer⁹ and

was continued by Nichols in the more general context of how failure modes are influenced by different environmental conditions¹⁰. Another mechanistic formulation was developed by Kiil, who simulated degradation of an epoxy-amine coating using a system of coupled differential equations for both chemical reaction rates and physical phenomena, such as the mass transfer of oxygen, water and volatiles^{8,11}.

One of the reasons why the simulation approach to photodegradation has gained so much interest, is related to the paradox that is often encountered in studies on service lifetime prediction: the research is focussed on the weathering of materials that are suitable for industrial applications, which means that they need to possess good stability against photodegradation, which in turn means that weathering tests take a long time to complete. Computer simulations hold high promise to circumvent this problem, especially when a variety of service environments is of interest for the material at hand. In addition, simulations may help to reduce economic and environmental costs, to which especially the savings on energy-consuming artificial exposure equipment can be a significant contribution. Finally, simulations can enable a researcher to study the effect of individual processes and stress factors on weathering, whereas experimental information is often generated from an overall combination of many stress factors, whose individual effects prove difficult to be separated.

Although there are important benefits of simulations in weathering research, polymer photodegradation is of such complexity that reliable experimental information will always be required. The optimal approach lies with the combination of experiment and simulation, thus making best possible use of their complementarity. In this article, we therefore develop a numerical method to simulate photodegradation of a cross-linked polymer coating and combine simulation with previously obtained experimental information on a degrading thermoset coating, in order to feed the simulations with experimental input data and to verify the simulation outcome with experimental results as well. In relation to the information

available from the experimental study, the simulations will be focussed on studying the same properties of the same coating system under the same exposure conditions: the depth-resolved evolution of optical properties and chemical composition of a polyester-urethane clearcoat during Weather-Ometer exposure. In the remainder of this article, the corresponding experimental study¹² will be denoted as the “experimental reference”.

Due to the complicated degradation chemistry of the polyester-urethane, a probabilistic approach is the most natural route, in our view, to simulate a system that can evolve via so many different chemical species, of which for some the (local) concentration can be very low. Therefore, a probabilistic simulation method based on a kinetic Monte Carlo (KMC) algorithm is developed for this purpose. For further information on the application of the KMC method in the framework of chemical reactions, also known as the Gillespie algorithm, the reader is referred to a previous publication by Makki et al.¹³. In that publication, a coarse-grained KMC degradation scheme was introduced, aimed at simulation of the weathering process of a crosslinked polymer on a nanometre scale. Such simulations provide valuable insights into the evolution of the network structure during photodegradation, but are, due to the complexity of such a degrading network, limited to small length scales and thus unable to display effects that appear on larger length scales, like inhomogeneity on a micrometre scale as was observed in the experimental reference. In the present article, a complementary KMC degradation scheme, dedicated to weathering simulations on larger length scales, is developed and applied to the simulation of photodegradation as studied in the experimental reference.

Although the simulations described in this article are specified towards polyester-urethane photodegradation, the general framework is equally suitable for the simulation of other (reaction) processes that occur in polymers, of which photocuring may be the most closely related example.

2 Modelling and simulation setup

2.1 Simulation volume

The desired weathering simulations require the ability to simulate coating volumes with a user-defined lateral size and thickness. The total simulation volume, denoted as “box”, represents a 3-dimensional coating volume, shaped as a rectangular cuboid of arbitrary dimensions (l_x, l_y, l_z) of which the z-direction corresponds to the coating thickness. This box is a spatially inhomogeneous element that can in principle describe inhomogeneity in all three dimensions. Next, the box volume is divided into (N_x, N_y, N_z) smaller elements in all three dimensions termed “cells”, whose centres are located at different positions (x, y, z) in the box. The cells serve as representative volume elements of the coating, implying that the conditions inside each individual cell are considered as spatially homogeneous. For convenience, the shape of a cell is (arbitrarily) chosen as a rectangular cuboid as well and all cells are of equal size. The definition of simulation volumes is schematically represented in Fig. 1.

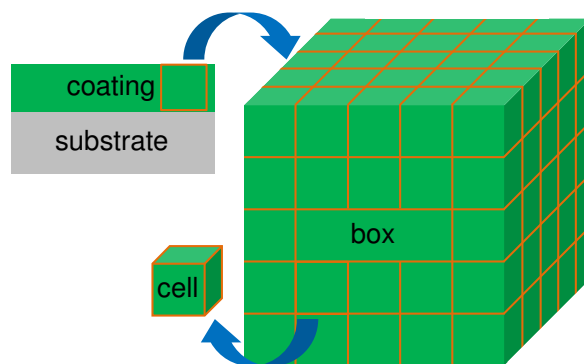


Fig. 1: Overview of the volumes defined for the simulation. A 3D volume of coating (box) is selected as the total volume of the simulation (top arrow). The spatially inhomogeneous box is divided into smaller elements: the spatially homogeneous cells (bottom arrow).

For a further definition of the system size, the size of a cell should be considered. The cell size should not be too small, as too few atoms may not be representative for a degrading network, nor should it be too large, as the cell size should be much smaller than the typical length scale of inhomogeneity. In addition, the cell dimensions also determine the spatial

resolution of the simulation in each direction. From several trials, it was found that a cell with a volume of the order of 1000 nm^3 contains sufficient material to be representative for simulating degradation and that a cell height of 100 nm is sufficiently small to capture the depth-inhomogeneity found in the experimental reference. After determining the cell dimensions, the desired coating area ($l_x \cdot l_y$) and thickness (l_z) of the simulation box can be adjusted via the number of cells that the box contains in each direction. Increasing the size of the simulation box leads to longer computation times to reach the same extent of degradation.

2.2 Coarse-grained model of the chemical structure

Simulation of a large box that contains an atomistically detailed description of the chemistry is unfeasible from a computational point of view. One part of this problem is due to the large number of atoms present per unit of volume, the other part is caused by the fact that all these atoms are interconnected via the topology of a specific network. A solution to this problem can be found by coarse-graining the molecular structure and by formulating a compositional description of the network.

Coarse-graining involves grouping clusters of atoms from the all-atom description of the molecular structure into superatoms, or beads¹⁴. The result of this operation is that the number of particles to be dealt with can be significantly reduced. Coarse-graining is a common procedure in the field of polymer simulations and has been applied to both thermoplastic¹⁴ and thermosetting systems¹⁵. The model polyester-urethane as used in this study was coarse-grained as shown in Fig. 2. The motivation for defining beads in this way will be clarified in the next sections.

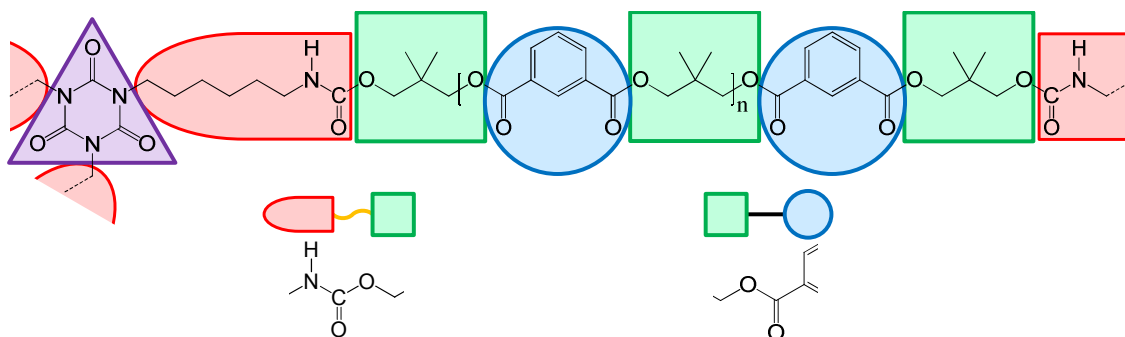


Fig. 2: Coarse-graining scheme used for the virgin polyester-urethane structure.

The material consists of the hydroxyl-functional polyester of isophthalic acid (IPA) and neopentylglycol (NPG) that is crosslinked with the trimer of hexamethyldiisocyanate (HDT). The polyester part is composed of two types of beads, originating from each one of its monomeric units: the IPA residue, which will be called “aromatic bead” (blue circle in Fig. 2) and the NPG residue, which will be called “aliphatic bead” (green square). The HDT crosslinker is also composed of two types of beads: the isocyanurate ring or “crosslinker body” (one per crosslinker molecule, purple triangle) and the isocyanate residue tail or “crosslinker arm” (three per crosslinker molecule, red bullet). Two bonds interconnecting the beads are modelled explicitly: the urethane bond (connecting crosslinker arm and aliphatic bead, yellow wiggly) and the ester bond (connecting aliphatic bead and aromatic bead, black bar). Coarse-graining the network, using beads instead of the atoms, already leads to a significant reduction (about 90%) in the number of entities to be dealt with. However, one can imagine that degradation chemistry, which, simplistically put, deals with breaking and making bonds, will still require an immense amount of bookkeeping by the simulation program due to the network topology. Breaking bonds at two different locations inside the same polymer chain results into two different network topologies. The same holds, for example, for the formation of new bonds and for tracking the locations of radicals in the network.

Keeping track of this network topology in every cell of a large box still makes simulation unfeasible. For this reason, a second simplification is performed by converting the chemical network with topology into a compositional representation of the network, without topology. In short, this step involves discarding all the connections between beads in the coarse-grained network representation, so that it is no longer known which individual beads are mutually connected, but instead the number of beads with a certain connection type is tracked. In order to retain the information of bonds inside a cell, it is necessary to include the number and type of connecting bonds inside the entity of each bead, or in other words, a representation of “beads with bonds” is needed. By following this scheme, the content of each cell in the box can now be represented by a simple composition vector \mathbf{C} that is used to count how many beads of each unique type are present in the cell. Analogously, the chemical composition of the whole box can be tracked by another composition vector \mathbf{B} , that contains all the cell composition vectors, such that $\mathbf{B} = [\mathbf{C}_1, \mathbf{C}_2, \dots, \mathbf{C}_N]$ with N the total number of cells in the box. The transition from topological network to compositional representation is schematically illustrated in Fig. 3 (please note that the bonds drawn in the compositional representation are actually “half-bonds”, with the other half belonging to a bead on the other side of the connection).

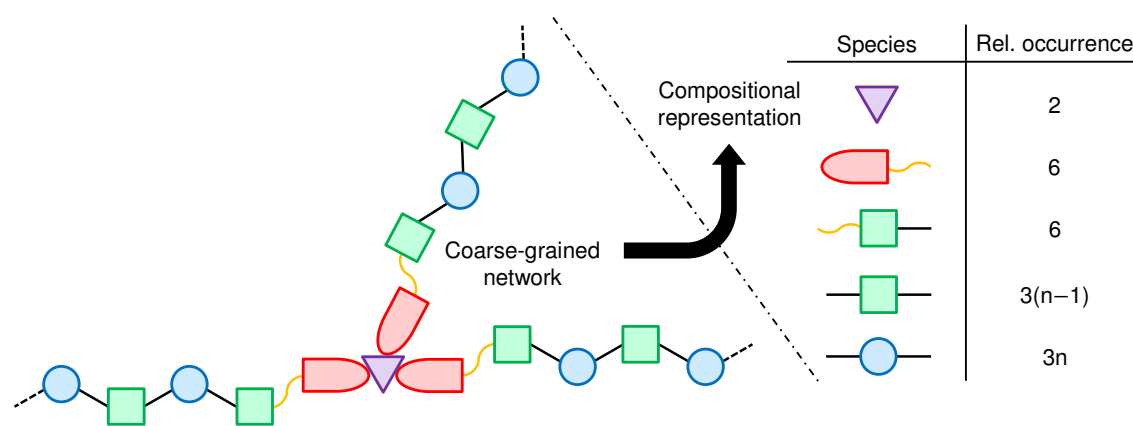


Fig. 3: Transition from the coarse-grained network with topology (left side) to the compositional representation of “beads with bonds” (right side). The right column of the table represents a vector \mathbf{C} that contains the (relative) cell composition for the virgin polyester-urethane.

From the table on the right side of the figure, it can be seen that the virgin cell is composed of only 5 different species (effectively only 4, as the isocyanurate ring can be considered inert during photodegradation, and therefore does not need to be tracked).

As mentioned earlier, the connectivity of a bead (number and type of bonds) is a property of each coarse-grained chemical species. Several other properties are attributed to each species as well, together defining its internal state. In order to efficiently implement internal states into the simulation later on, an integer number, called the “stateID”, is assigned to every unique species that can be present in the simulation box. The values of each individual property are coded by an integer number as well. In Table 1, the attributed bead properties are collected.

Table 1: Overview of bead properties and related information.

Property	Short description	Value range	Relevant for bead types
type	Type of coarse-grained entity	0-3	all
absorptivity	Photon absorptivity state	0-1	aromatic
oxidation_state	Extent to which a bead is oxidised	0-2	aliphatic, crosslinker arm
n_ester_bonds	Number of connecting ester bonds	0-2	aromatic, aliphatic
n_urethane_bonds	Number of connecting urethane bonds	0-1	aliphatic, crosslinker arm
n_newxl_bonds	Number of new crosslink bonds (C-C)	0-3	aromatic, aliphatic
n_radicals	Number of radicals on a bead	0-1	all

A unique stateID is thus assigned to any fixed combination of property states, as coded by the numbers in the third column of Table 1, and vice versa, a unique set of property states can be recovered from each stateID. The “type”-property of a species is the main criterion that determines the role of that bead in the photodegradation process, as the type determines whether the bead is an aromatic bead, an aliphatic bead, a crosslinker arm bead or a void in the coating, where this last bead type results from the removal of a bead of any of the other bead types from the cell. According to a bead’s type, some of its properties may or may not be relevant (last column in Table 1). For example, the absorption of photons is attributed to the aromatic moieties of PNI and hence the “absorptivity”-property is only relevant for the aromatic beads. Similarly, the hydrogen atoms that can be most easily abstracted from the network are located adjacent to the ester and urethane bonds in the coating. Radicals will

therefore most likely be located at these sites, making those locations in the material the most likely ones for oxidation reactions. For that reason, the “oxidation_state”-property is relevant for aliphatic beads and crosslinker arm beads only. Additional information regarding bead properties and associated property values can be found in the next section, where they will be discussed in the context of photodegradation reactions.

Eventually, the degraded coarse-grained composition, as obtained from the simulations, can be represented as an atomistically detailed composition, via a procedure denoted as fine-graining. This conversion requires definition of a representative molecular structure for each coarse-grained species present after degradation. This fine-graining procedure, which allows for more detailed insight on the atomistic level, will be discussed in a future publication.

2.3 Coarse-grained model of photodegradation reactions

The composition of each cell in the coating is tracked by a composition vector \mathbf{C} that initially contains four nonzero entries, that is, the number of beads in the cell for each of the four reactive stateID's in the virgin coating (see Fig. 3). During the simulation, beads disappear (reactants) and beads with other stateID's form (products). In total, about 90 different stateID's can be found in the simulations. To simulate compositional evolution via these species, the possible steps for a species to evolve, called “reaction mechanisms”, have to be defined. In order to obtain a realistic outcome of the simulation, these mechanisms should obviously be (coarse-grained) models of degradation reactions that occurs in reality. Although the detailed degradation chemistry of urethane-crosslinked PNI is very complicated and surely not completely known and understood, one can still try to capture its main pathways and define reaction mechanisms according to that knowledge. Based on experimental results available from literature and as obtained in the experimental reference, the list of reaction mechanisms in Table 2 was compiled. The last column in the table reflects

the order of each reaction mechanism in the reactant beads, with the reaction order in the radical reactant beads in parentheses.

Photodegradation is initiated by the generation of radicals as a consequence of photon absorption. Previous work on the (molecular) degradation mechanisms of PNI has shown that the initiation step for this material is of a photolytic nature, more specifically by Norrish type I photocleavage of the aromatic ester group¹⁶. The scission mechanism in Table 2 represents this initiation step.

Table 2: Reaction mechanisms defined for the simulations.

Mechanism name	Description	Reaction order
<i>Initiation</i>		
scission	Photolytic scission of an ester bond	1
<i>Propagation</i>		
abstraction-H_ali	Hydrogen abstraction from an aliphatic bead	2 (1•)
abstraction-H_xl	Hydrogen abstraction from a crosslinker arm bead	2 (1•)
evaporation_ali	Evaporation of a maximally oxidised aliphatic bead	1
evaporation_xl	Evaporation of a maximally oxidised crosslinker arm bead	1
leaching	Leaching out of aliphatic beads without any connecting bonds left	1
oxidation	Oxidation of an aliphatic or crosslinker arm bead with a radical (a urethane bond is broken if a crosslinker arm bead is oxidised)	1 (1•)
<i>Termination</i>		
grafting	Grafting between two aromatic beads forming a new crosslink	2 (1•)
recombination_aro	Recombination of two aromatic radicals forming a new crosslink	2 (2•)
recombination_ali	Recombination of two aliphatic radicals forming a new crosslink	2 (2•)
sink_aro	Loss of aromatic radicals due to unknown reactions (sink)	1 (1•)
sink_ali	Loss of aliphatic radicals due to unknown reactions (sink)	1 (1•)

Numerous propagation mechanisms are known for the photodegradation of this type of polyester-urethanes. Radicals generated by ester bond photolysis can travel through the material via hydrogen abstraction reactions^{16,17}. Because of the stability of the radical formed after abstraction, two sites have the largest probability to be successfully attacked by a radical: the methylene hydrogen atoms in the α -position to the ester bond and those in the α -position to the NH of the urethane bond, of which the latter methylene hydrogen atoms are the most weakly bound¹⁸. These two reactions are represented by the two hydrogen abstraction mechanisms in Table 2. In the presence of oxygen, radicals in the material can react with it (that is, get oxidised), enabling a large variety of follow-up reactions to occur. A

peroxy radical is formed in the α -position to the ester bond, which in turn can be converted, for example into a hydroperoxide, by hydrogen abstraction. Via different routes, such (labile) hydroperoxides may lead to the formation of several oxidised chemical groups, including anhydrides, acids and hemiacetals, sometimes accompanied by chain breaking reactions¹⁶. Similarly, hydroperoxides can be formed in the α -position to the urethane bond NH, followed by conversion into an acetylurethane function that can be hydrolysed by water formed *in situ*, ultimately leading to breakage of the urethane link into a carboxylic acid and a urethane end group¹⁸. The formation of oxidised structures is represented in the simulation via the oxidation mechanism. Progressive oxidation can lead to the formation of volatile fragments (such as CO₂), that may evaporate from the coating. These processes are represented by the two evaporation mechanisms in Table 2. Aliphatic units that are no longer connected to the network, such as neopentylglycol or oxidised derivatives thereof, may leach out of the coating via the leaching mechanism (in reality, one could also think of washing out by water, for example).

Finally, several termination reactions in which radicals are consumed are taken into account. Phenyl radicals, that can form after ester bond photolysis, have been shown to “graft” to other isophthalic moieties of PNI chains¹⁷, which is represented by the grafting mechanism in the simulations. Additionally, two phenyl radicals may recombine to form a new C-C bond, described by the aromatic recombination mechanism in the simulation. A similar recombination reaction may take place between two aliphatic radicals, also resulting in a newly formed crosslink, via the aliphatic recombination mechanism. Recombination reactions between aliphatic and aromatic radicals have been omitted for simplicity. The list from Table 2 is concluded by adding two more mechanisms (radical sinks) that account for radicals in the experimental system that are lost due to other processes, for example, the encountering of defects and impurities.

The possible degradation pathways that *may* be followed in the simulation are now set by the list of defined reaction mechanisms. The questions that remain to be answered are about the pathways that *will* be followed when a virgin system evolves into a degraded system under given boundary conditions, and about the importance of every mechanism during such a degradation process. In order to answer those questions, the setup of the simulation scheme will be completed in the following two sections, in which reaction rates are introduced and some algorithmic details of the KMC simulations are discussed.

2.4 Photon absorption and degradation rates

Because initiation of the photodegradation process is directly related to the absorption of UV radiation, a proper modelling of photon absorption by the coating is an essential requirement for the KMC simulation. As mentioned earlier, photon absorption is attributed to the aromatic moieties of PNI, that is, to the aromatic beads in the simulation box. Two types of absorbing beads are distinguished: aromatic beads that are not connected to another aromatic bead (“monophenyls”), which is the case for all aromatic beads in the virgin coating, and aromatic beads that are connected to another aromatic bead (“biphenyls”). The difference between these two types is that biphenyls absorb a larger fraction of the incident photon flux than monophenyls do, in reflection of their extended conjugation of excited states. The formation of biphenyl species is therefore used to model the increase of the coating absorptivity as degradation proceeds, mainly the formation of an absorption tail at wavelengths of 300 nm and higher (as discussed in the experimental reference). Please recall that biphenyl structures may form via the grafting as well as the aromatic recombination mechanisms.

When the top of a cell is irradiated with UV light, every aromatic bead in that cell will absorb a portion of the incident photon flux. Unless the cell height becomes extremely large, the absorbed fraction will always be (much) smaller than 1, meaning that a finite photon flux will leave the cell on the bottom side. The flux that leaves one cell will consequently be the

incident flux for the next cell it encounters. This is the way in which photon absorption is implemented in the simulation of a box of cells. The irradiation flux will here be considered to enter the box normal to its (x,y)-surface at $z = 0$, which corresponds to irradiation of a coating volume perpendicular to its surface and, of course, from the top. Calculation of the photon flux profile throughout the depth of the box, that is, throughout the coating thickness, is therefore performed column-wise. Each column of cells (constant x and y) has its own photon flux profile and the total photon flux leaving the very bottom of the box can be obtained by summation of the individual photon fluxes that leave every cell in the bottom layer. In this way, any (chemical) inhomogeneity that may form in the lateral dimensions of a coating can also be reflected by laterally inhomogeneous photon absorption in the simulation box.

Next, reaction rates for the KMC method need to be defined. Because the cell is a spatially homogeneous element that can be considered as a tiny batch reactor, standard chemical reaction rate equations are applied in which the chemical composition of the cell will be the driving force for certain reactions to be preferential above others. For most reaction mechanisms listed in Table 2, the rate equation for a specific reaction of species i (or species i and j in case of a second order reaction) within reaction mechanism m is given by

$$r_i[\text{h}^{-1}] = k_m[\text{h}^{-1}]N_i \quad (1)$$

for a first order reaction and by

$$r_{ij}[\text{h}^{-1}] = \frac{k_m[\text{m}^3\text{h}^{-1}]}{V_{\text{cell}}[\text{m}^3]}N_iN_j \quad (2)$$

for a second order reaction, with r the reaction rate, k the rate constant associated with the mechanism, N the number of the reactant species in the cell and V_{cell} the cell volume. The time scale is expressed in hours for easy comparison with the experimental degradation time.

For certain mechanisms, the rate expressions are slightly more complicated compared to those of equations (1) and (2). In the hydrogen abstraction mechanism for aliphatic beads, a

weight factor is included to take into account the number of hydrogen atoms that can be abstracted from the aliphatic reactant (and hence the relative probability for abstraction). In the oxidation mechanism, the local concentration of oxygen is incorporated into the rate equation. For the two recombination mechanisms, a combinatorial factor is included to account for the situation that $i = j$, as two beads with the same stateID can participate in the recombination reaction. A noticeable exception to the general form of rate equations discussed so far is found for the ester bond scission mechanism, caused by the fact that it requires a direct coupling to the rate of photon absorption. Without further explanation, the equation used to compute the rate of a scission reaction is given by

$$r_{ij}[\text{h}^{-1}] = \phi[\text{m}^{-2}\text{h}^{-1}]\sigma_i[\text{m}^2]N_i \frac{N_j N_{\text{est},j}}{\sum_k (N_k N_{\text{est},k})} q_{ij} \quad (3)$$

and

$$q_{ij} = 1 - (1 - q)^{N_{\text{est},i}} \quad (4)$$

where the labels i , j and k refer to aromatic, aliphatic and all types of beads, respectively, and with ϕ the photon flux entering the cell, σ the bead's absorption cross-section, N_{est} the number of ester bonds and q the quantum efficiency of photolysis.

Photodegradation rates generally depend on temperature, regarding both chemical processes (e.g., reaction rate constants) and physical processes (e.g., diffusion coefficients, solubility values). If the temperature dependence of all the processes involved would be known, temperature could be explicitly included into the simulation scheme. However, because such information generally is not available, the simulations in this article represent a constant temperature condition, namely, that of the experimental reference (WOM exposure at a black standard temperature of 65 °C)¹².

2.5 Incorporation of oxygen solubility and diffusion into the KMC scheme

There are multiple routes to incorporate the diffusion of oxygen into the KMC simulation scheme. In order to make a smart choice on how to do so, it is helpful to first make an estimate of how much oxygen can actually be expected to be present. The solubility S of oxygen in comparable polymers is typically¹⁹ $0.05\text{-}0.1\text{ cm}^3(\text{STP})\text{cm}^{-3}\text{bar}^{-1}$. For a polymer in air ($p_{\text{O}_2} = 0.21\text{ bar}$), this translates into $0.4\text{-}0.8\text{ mol}\cdot\text{m}^{-3}$, or $(0.8\text{-}2)\cdot 10^{-3}\text{ m}\%$. When compared to the bead number density in the simulation, this means that in the fully saturated coating, roughly 1 oxygen molecule is present per 10,000 reactive beads. With this information at hand, one can imagine that the explicit incorporation of oxygen as a bead that can traverse cell boundaries via a diffusion process may lead to a rather unstable reaction-diffusion equation system with an oxygen concentration profile that will evolve in a rather spiky fashion with many computationally inefficient “back-and-forth” diffusion jumps. Instead, it seems better to model oxygen implicitly, that is, as an effective cell property, and to use an implicit solution scheme to solve the reaction-diffusion equations. This implicit reaction-diffusion scheme for the oxygen concentration is described in Supporting Information 1.

This choice has an important consequence for the incorporation of oxygen diffusion into the KMC simulation scheme, because now a time-driven process (implicit oxygen diffusion) has to be included into the simulation that, so far, was purely event-driven. The integration of these two types of processes was performed in the following way:

1. A constant step time for diffusion, t_{diff} , is defined in addition to the cumulative time scale of the simulation, t_{exp} ;
2. The KMC scheme is followed as usual, until t_{exp} has progressed for one block of time with a length equal to t_{diff} ;

3. When the condition from 2. is met, the system of reaction-diffusion equations (which is a matrix equation) is solved with the actual conditions of the degrading box just before passing into the next block of t_{diff} ;
4. The conditions for each cell are updated with the new oxygen concentration profile that follows from solving the matrix equation and consequently, all oxidation rate equations are updated as well;
5. Degradation continues until the condition from item 2 is met again.

It is important to emphasise that the reaction that will occur right after the diffusion update is already selected just before the diffusion update takes place, although execution of this reaction is of course performed after the diffusion update. In this manner, one can assure the possibility for selection of reactions with a relatively low rate. Otherwise, the probability for selecting a slow reaction can effectively become zero due to expulsion by oxidation rates that are continuously refuelled by oxygen diffusion, which would violate the KMC principle that each reaction with a finite rate has a finite probability to occur. Because the reaction to perform after the update is selected before updating, it is also possible that the corresponding Δt for that reaction equals or exceeds $2t_{\text{diff}}$. If that is the case, the required number of diffusion updates is performed consecutively by solving the reaction-diffusion equations multiple times with iteratively updated oxygen profiles. Another advantage of an implicit scheme for oxygen diffusion is that it generates stationary solutions for the oxygen concentration gradient and is therefore rather insensitive to the value of the diffusion time step. As long as t_{diff} is sufficiently small with respect to the time scale of degradation reactions, the evolution of the simulation is not influenced by its precise value. The rather arbitrary value of 1 h was used as the diffusion time step for the simulations.

2.6 KMC simulation setup

It is convenient to distinguish different levels of degradation rates. In the first place, any of the rates r_i or r_{ij} from equations (1)-(3) represents the rate of an individual reaction of stateID i (and, if applicable, stateID j) in a single cell, governed by the concentrations of the reactants involved and the rate constant of the mechanism to which the reaction belongs. One level higher consists of the sum of all individual reaction rates r_i and r_{ij} within that reaction mechanism in the same cell (cell mechanism rates). Again one level higher consists of the sum of all reaction mechanism rates, still within the same cell (cell degradation rates). The final level is the total or box degradation rate, which is the sum of all cell rates. This hierarchical structure is used for selecting individual reactions and time delays between subsequent reactions in the KMC scheme. For those purposes, relative reaction rates are treated as relative probabilities: if the rate of reaction A is two times higher than the rate of reaction B, then the probability that reaction A is selected to occur next is two times higher than the probability that reaction B is selected. From the hierarchical build-up, one can imagine how this works exactly the same on all levels: a single random number draw determines in which cell the reaction occurs, within which mechanism it occurs and finally which individual reaction occurs.

From this setup, a general KMC algorithm is followed to perform the simulations. Reaction rates that change due to a change in composition are continuously updated to their actual values. This also holds for the rates of photon absorption and scission in the cell that hosted the latest reaction event and in all cells in the same column below that cell (recall section 2.4). The program continues looping until the desired extent of degradation has been reached (user-defined criterion) and regularly provides output that can be analysed after the simulation completes.

Although the developed simulation method is capable of describing inhomogeneous behaviour in three dimensions, the inhomogeneity that will result from the degradation model as it is implemented here, is mainly inhomogeneity in the depth-dimension (due to light attenuation, for example). In addition, also the results from the experimental reference that are to be simulated were obtained in a depth-resolved fashion. For the sake of efficiency, simulations were therefore performed on a single column of cells only (that is, $N_x = N_y = 1$). Justification of this choice was obtained from observing that simulation of a box composed of a single column gives the same result as simulation of an equally sized box with many columns after layer-wise averaging of the results. The simulation results described in the remainder of this article are therefore focussed on depth inhomogeneity only.

Constant cell dimensions of $(17.4 \cdot 17.4 \cdot 100) \text{ nm}^3$ were chosen for the simulations. This cell volume, which is quite a bit larger as compared to the 1000 nm^3 that was mentioned before, was chosen for the advantage that including more material into a cell leads to smaller fluctuations in the simulated depth profiles. Each modelled PNI chain has a polymerisation degree of 4, so that there are 9 beads in between two crosslinker arm beads and the ratio [ester bonds/urethane bonds] equals 4. The composition of a single representative network element, as displayed in the table of Fig. 3, is multiplied 4140 times within each cell, leading to an overall mass density of $0.94 \text{ g}\cdot\text{cm}^{-3}$, which corresponds to what was obtained from MD simulations¹³. Initially, each cell contains 136,620 reactive beads, 99,360 ester bonds and 24,840 urethane bonds. As mentioned before, the simulated coating thickness can be adjusted via the number of cells in the z-direction of the box. The simulated evolution of the depth-resolved composition during degradation can depend on the chosen coating thickness: for example, the presence of an impermeable substrate at a certain depth in the box may influence the oxygen concentration profile $C_{O_2}(z, t)$ during the simulation, which in turn influences the rates of degradation reactions.

All simulation code was written in an object-oriented programming language (C++) to optimise the computational efficiency of the program. Selection algorithms used in the KMC procedure were based on binary tree data structures. The Boost #mt11213b random number generator²⁰ was used to draw two independent random numbers for computing the event time and selecting an event. Reaction-diffusion equations were solved using the SimplicialLDLT-solver from the SparseCholesky-module of the Eigen library.

3 Results and discussion

3.1 Spectral dependence and simulation parameters

From the results described in the experimental reference¹², it was found that degradation of coatings as a result of Weather-Ometer (WOM) exposure occurred in an inhomogeneous fashion throughout the depth of a coating, with respect to both the optical and the chemical changes. The cause for this depth inhomogeneity was found in the different penetration depths of photons present in the WOM irradiance spectrum. In order to simulate degradation during WOM exposure, this wavelength dependence of the penetration depth should be taken into account as well. Based on considerations that can be found in Supporting Information 2, the spectrum was split into two regimes: the short wavelengths (270-294 nm), labelled “S” and the long wavelengths (294-334 nm), labelled “L”.

Based on this split-up, the parameters for simulation of WOM degradation that could be determined *a priori* are reported in Table 3. The other simulation parameters are initially unknown values that have been optimised to give the best possible description of the experimental data. How this optimised parameter set, that will be referred to as $[P_{\text{opt}}]$, was established, will be discussed in section 3.6. The content of $[P_{\text{opt}}]$ is shown in Table 4 (the distinction between primary and secondary rate constants will also be discussed later).

Table 3: Fixed simulation parameters used to simulate WOM degradation.

Parameter name	Symbol	Value	Unit	Calculated from
Irradiance_S	$\phi_{\text{eff,S}}$	$4.361 \cdot 10^{20}$	$\text{m}^{-2}\text{h}^{-1}$	$\int_{270 \text{ nm}}^{294 \text{ nm}} d\lambda \Phi(\lambda)$
Irradiance_L	$\phi_{\text{eff,L}}$	$4.543 \cdot 10^{22}$	$\text{m}^{-2}\text{h}^{-1}$	$\int_{294 \text{ nm}}^{334 \text{ nm}} d\lambda \Phi(\lambda)$
AbsCrossSec0_S	$\sigma_{0,\text{eff,S}}$	$2.498 \cdot 10^{-22}$	m^2	$\frac{1}{\rho_0} \frac{\int_{270 \text{ nm}}^{294 \text{ nm}} d\lambda \Phi(\lambda) \alpha_0(\lambda)}{\int_{270 \text{ nm}}^{294 \text{ nm}} d\lambda \Phi(\lambda)}$
AbsCrossSec0_L	$\sigma_{0,\text{eff,L}}$	$1.516 \cdot 10^{-24}$	m^2	$\frac{1}{\rho_0} \frac{\int_{294 \text{ nm}}^{334 \text{ nm}} d\lambda \Phi(\lambda) \alpha_0(\lambda)}{\int_{294 \text{ nm}}^{334 \text{ nm}} d\lambda \Phi(\lambda)}$
AbsCrossSec1_S	$\sigma_{1,\text{eff,S}}$	$= \sigma_{0,\text{eff,S}}$	m^2	-

Table 4: Optimised parameter set [P_{opt}] used to simulate WOM degradation.

Parameter name	Symbol	Value	Unit
<i>Primary rate constants</i>			
k_evaporation_ali	$k_{\text{eva,ali}}$	$1.020 \cdot 10^{-3}$	h^{-1}
k_sink_ali	$k_{\text{sink,ali}}$	$1.013 \cdot 10^{-3}$	h^{-1}
k_oxidation	k_{ox}	$1.593 \cdot 10^{-3}$	m^3h^{-1}
k_abstraction-H_ali	$k_{\text{absH,ali}}$	$0.757 \cdot 10^{-29}$	m^3h^{-1}
k_abstraction-H_xl	$k_{\text{absH,xl}}$	$0.864 \cdot 10^{-29}$	m^3h^{-1}
k_grafting	k_{graft}	$2.549 \cdot 10^{-29}$	m^3h^{-1}
k_recombination_ali	$k_{\text{rec,ali}}$	$2.105 \cdot 10^{-29}$	m^3h^{-1}
<i>Secondary rate constants</i>			
k_evaporation_xl	$k_{\text{eva,xl}}$	$1 \cdot 10^{-3}$	h^{-1}
k_leaching	k_{leach}	$1 \cdot 10^{-3}$	h^{-1}
k_sink_aro	$k_{\text{sink,aro}}$	$1 \cdot 10^{-3}$	h^{-1}
k_recombination_aro	$k_{\text{rec,aro}}$	$2 \cdot 10^{-29}$	m^3h^{-1}
<i>Other parameters</i>			
AbsCrossSec1_L	$\sigma_{1,\text{eff,L}}$	$1.826 \cdot 10^{-23}$	m^2
QuantumEff_sci	q	$0.752 \cdot 10^{-3}$	-
DiffCoeff_oxygen	D_{O_2}	$4.353 \cdot 10^{-10}$	m^2h^{-1}
SatConc_oxygen	$C_{\text{O}_2,\text{sat}}$	0.990	$\text{mol} \cdot \text{m}^{-3}$

3.2 Simulation of degradation for a thin coating

The degradation of thin coatings during WOM exposure was simulated by performing KMC simulations using [P_{opt}] with a stack of 40 cells, which corresponds to a coating thickness of 4 μm . This case is comparable to the coatings that were degraded to perform FTIR and UV-VIS transmission spectroscopy measurements in the experimental reference. There are three observables for which experimental and simulation results can be directly compared:

the remaining fraction of ester bonds, the remaining fraction of urethane bonds (chemical comparison) and the absorbance in the long-wavelength regime (optical comparison). These results* are shown and compared in Fig. 4. In order to relate the simulation outcome to thin coating degradation, it was also analysed as if it were a transmission measurement, that is, the result for the box as a whole was calculated.

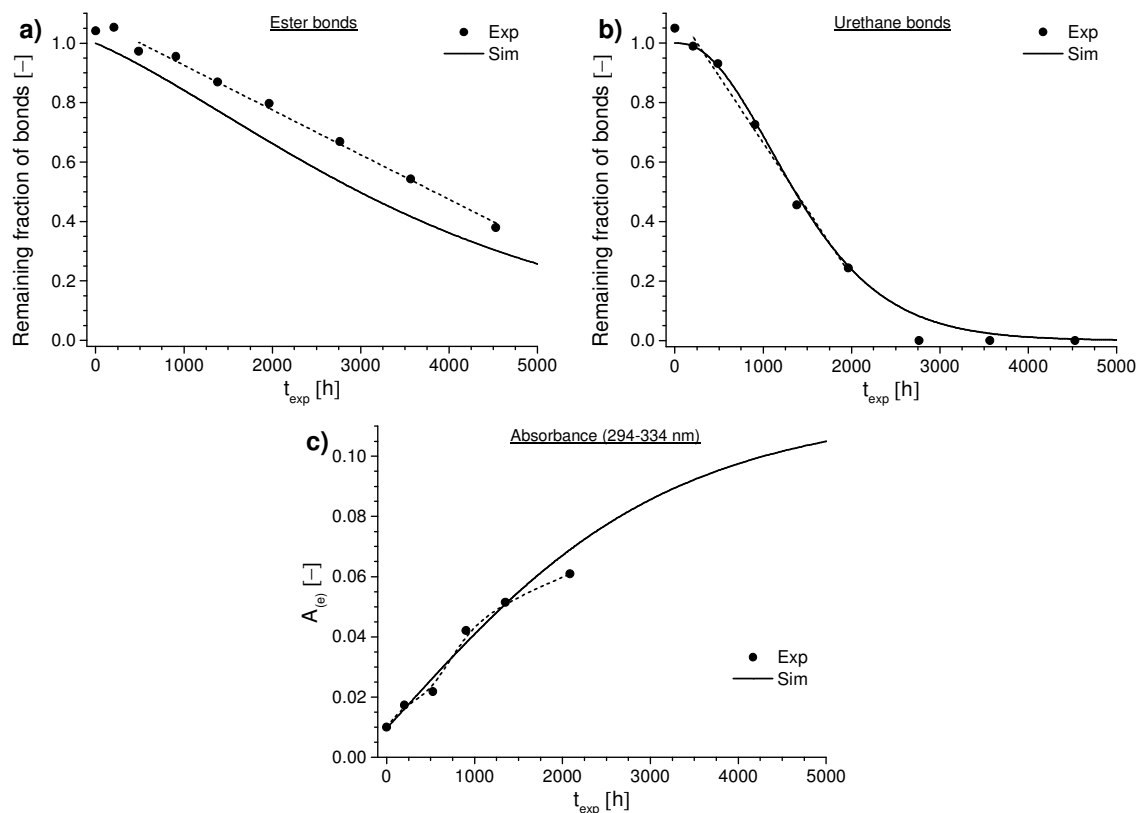


Fig. 4: Comparison between experimental (circles and dashed lines) and simulation results (solid lines) for WOM degradation of a thin coating, for a) ester bonds, b) urethane bonds and c) absorbance of the long wavelength regime (n.b.: the absorbance based on the natural logarithm of the transmittance, $A_{(e)}$, is plotted).

Simulation results of the urethane bond fraction (Fig. 4b) and the long wavelength absorbance (Fig. 4c) match well with the experimental data for the available time window. When the experimental and simulation results for the ester bond fraction are compared (Fig. 4a), it can be seen that the simulated rate of scission is rather constant with time and its

* The experimental data shown in Fig. 4a and b are the surface concentration values from the experimental reference (Fig. 14, solid black symbols) because these data yield the most suitable comparison for simulation of both thin and thick coatings with a single parameter set.

absolute value, the slope of the curve, matches quite well with its experimental counterpart. However, there is an offset between the experimental and the simulated time evolution. This offset is due to the experimental data points that remain slightly above a value of 1.0 for about the first 500 hours of exposure. Experimental reasons for this behaviour are a combination of i) the accuracy of the FTIR data (measurement factor), ii) the possibility that the quantified FTIR signals arise majorly but not entirely from the bonds that they have been assigned too (interpretation factor) and iii) the fact that coating degradation at the very beginning of an exposure experiment is inherently not well understood (material degradation factor). A chemical explanation related to the latter two reasons could be, for example, the presence of a small amount of stabilisers, such as phenolic antioxidants that are often used to prevent degradation during the synthesis of polyester resins. Residual stabilisers may be degraded first, before the resin itself starts to experience significant degradation and degradation products of such stabilisers may interfere with the FTIR signals of the resin as well. From the definition of the degradation mechanisms, it obviously follows that such an onset behaviour cannot result from the simulations, as initiation results from the breakage of ester bonds via the scission mechanism. Only when an initial amount of radicals is formed by breaking a certain fraction of ester bonds, the other mechanisms will be fuelled with a sufficient number of reactants to become equally significant to or dominant over the scission reactions.

Because the experimental and simulated “lines” from Fig. 4a are approximately parallel, the best comparison between experiment and simulation with respect to the remaining fraction of ester bonds is perhaps to compare the simulation outcome to the experimental results minus a constant value (the offset that exists due to the experimental start-up period). This comparison between the simulated ester bond fraction and the “shifted ester bond fraction” from experiment, will be made in the next two sections that deal with the

degradation of thick coatings. As a final remark on the results from Fig. 4a, it has also been observed that a constant rate of scission with increasing exposure time can only result from the simulation if the evolution of the optical properties (Fig. 4c) matches closely with the experimental data. Any (large) discrepancy between simulated and experimental evolution of the long wavelength absorbance leads to strongly nonlinear results for the simulated evolution of the ester bond fraction. This observation confirms the importance of a correct coupling between chemical reactions (photolysis) and optical properties (photon absorption) that has been discussed in the experimental reference.

3.3 Simulation of degradation for a thick coating I: constant oxygen condition

The degradation of thick coatings during WOM exposure was simulated by performing KMC simulations using $[P_{\text{opt}}]$ with a stack of 400 cells, which corresponds to a coating thickness of 40 μm . This case is comparable to the samples used for depth-resolved infrared microscopy measurements in the experimental reference. The simulation was performed using constant oxygen conditions, that is, during the entire simulation, the oxygen concentration in each cell is kept constant at a value equal to its saturation concentration ($C_{\text{O}_2,\text{sat}}$). In practice, this condition was maintained by setting the diffusion coefficient to a very high value. The experimental and simulated depth-resolved evolution of the remaining fraction of (shifted) ester bonds and urethane bonds are shown in Fig. 5.

The overall match between experiment and simulation for the ester bond fraction after shifting (Fig. 5a) is quite good, especially for the intermediate exposure times (1380-2760 hours). The surface fractions match well (as would also be expected from comparison to Fig. 4a) and also the development of the gradients in approximately the upper 20 μm is captured decently. Only the experimental bulk levels do not compare very well to their simulated counterparts. Apparently, the significant simplification of representing a complete spectral dependence by only two wavelength packages does not impede a proper description of the

depth-resolved scission behaviour: evolution via specific gradients in the upper portion of the coating, accompanied by a steady decrease of the bulk level.

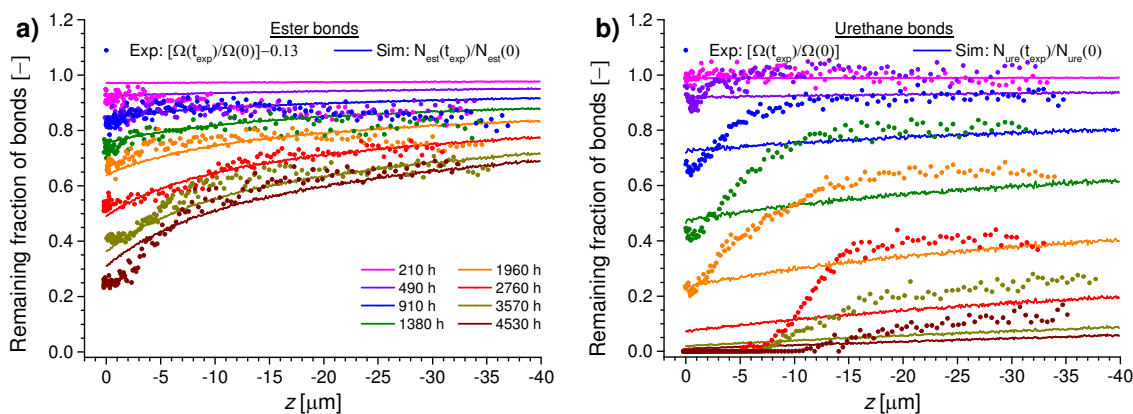


Fig. 5: Comparison between depth-resolved experimental (circles) and simulation results (lines) for WOM degradation of a thick coating, for a) (shifted) ester bonds and b) urethane bonds. Different colours represent different exposure times.

For the urethane bond fraction (Fig. 5b), there is quite a difference between experiment and simulation. The progression of the experimental surface fraction is well described by the simulation, but the concentration gradients in depth and the bulk fractions have a poor match. Looking back at the degradation mechanisms, one finds that urethane bonds are broken as a result of oxidation reactions. In the simulation scheme applied so far, a gradient in the remaining fraction of urethane bonds should therefore be related to a gradient in the concentration of radicals that can be oxidised, due to the fact that the oxygen concentration in each cell was kept constant. In Fig. 6, the evolution of the radical bead fraction for the same simulation is displayed. The radical concentration profiles do evolve via gradients with a shape as expected from the ester bond gradients (Fig. 5a), that is, a larger concentration at the surface as compared to the bulk. The magnitude of these gradients is, however, apparently insufficient to account for such steep gradients in the urethane bond concentration (at 1380 h, for example, the surface concentration of radicals is only 50% larger than the bulk level).

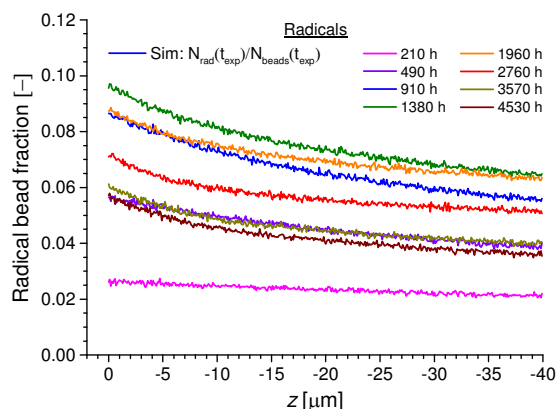


Fig. 6: Depth-resolved simulation results for WOM degradation of a thick coating, for the radical bead fraction.

Another obvious factor that governs oxidation reactions is the availability of oxygen. For this simulation, the oxygen concentration in every cell was kept constant at a value that only reflects saturation conditions, that is, to take the partial pressure of oxygen in the degradation environment into account. In reality, oxygen can only enter the coating from the surface, which means that if it is consumed by oxidation reactions inside the coating, it should be replenished via a diffusion process. The limitation in the diffusion of oxygen may account for an additional gradient, that of the oxygen concentration, which can affect the in-depth behaviour of oxidation reactions as well. In the next section, the diffusion of oxygen will therefore be included into the simulation to study the effect of describing the oxidation reactions via a coupled reaction-diffusion process (for details, please see Supporting Information 1).

3.4 Simulation of degradation for a thick coating II: diffusing oxygen condition

The simulation with the settings from the previous section was repeated, but now with inclusion of oxygen diffusion as described in section 2.5. The initial condition was the same as for the simulation in the previous section, but for the simulation discussed here, the oxygen concentration in each cell was left free to change. Both the diffusion coefficient and the saturation concentration (the maximal value for the oxygen concentration) were kept constant for each cell. The experimental and simulated depth-resolved evolutions of the remaining

fraction of urethane bonds and the simulated oxygen concentration profiles are shown in Fig. 7 (the influence on the ester bond result is negligible and hence the outcome for this bond is equal to what was shown in Fig. 5a).

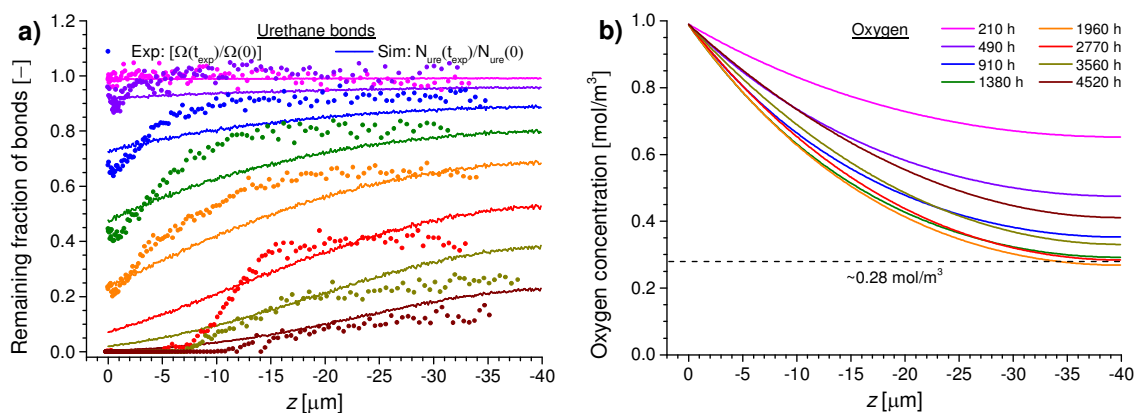


Fig. 7: Simulation results for WOM degradation of a thick coating including oxygen diffusion, that show a) the comparison between depth-resolved experimental (circles) and simulation results (lines) for the urethane bonds and b) the simulation results for the oxygen concentration.

Compared to Fig. 5b, the simulated urethane bond gradients from Fig. 7a match quite a bit better than in the case of the constant oxygen concentration. For the intermediate exposure times, both the simulated surface and bulk concentrations progress in line with the experimental data. The magnitude of the gradients (steepness) in the upper $\approx 15 \mu\text{m}$ of coating is also getting closer to the experimental results, although the simulated gradients do still not change as steeply as their experimental counterparts. This observation will be discussed in some more detail in section 3.6. A similar steep gradient as observed for the experimental data used here resembles the gradients found by Erich et al.²¹ and Laven et al.²² for alkyd films that convert chemically by oxygen that diffuses into the film.

The oxygen concentration gradients, shown in Fig. 7b, reveal that the local concentration of oxygen indeed plays an important role in the depth-inhomogeneity of oxidation reactions. With increasing exposure time, first a concentration gradient with increasing steepness is formed, which then stabilises during intermediate exposure times and later again starts to flatten towards the equilibrium situation of homogeneous saturation, because the system is

running out of reactants that can be oxidised. The formation of a stable concentration gradient for intermediate exposure times was also observed for simulations in which the oxygen-related parameters (D_{O_2} and $C_{O_2,sat}$) were varied with respect to $[P_{opt}]$. The level of the stabilised oxygen concentration in the bulk of the coating (dashed line in Fig. 7b) can be tuned with these parameters and is, not very surprisingly, directly correlated to the oxidation rate and thus to the evolution of the urethane bond concentration in the bulk.

3.5 Sensitivity analysis and parameter interpretation

The effect of each of the model parameters in $[P_{opt}]$ on the simulation outcome was studied in some detail. The simulation as presented in section 3.4, of a thick coating including oxygen diffusion, was selected as the system of study. From the full time evolution, one intermediate exposure time (1960 h, orange data in Fig. 7a) was chosen to base the sensitivity analysis on. The individual influence of each of the 15 parameters p in $[P_{opt}]$ on 5 different observables y was studied. These 5 observables are the urethane bond fraction at the surface, the urethane bond fraction in the bulk, the slope of the urethane bond gradient, the ester bond fraction at the surface and the ester bond fraction in the bulk. Mathematical criteria, such as averages or the intercepts and slopes of linear fits, were defined for all these observables, so that they could be determined unambiguously from the simulation outcome.

The value of each parameter p_i was increased (multiplication by a factor f_i) and decreased (multiplication by a factor f_i^{-1}), where the magnitude of f_i that was chosen depends on the sensitivity of the observables to the parameter (this was a trial-and-error process). The response R_{ij} of each observable to each parameter was quantified as

$$R_{ij} = \Delta y_j / (2\Delta \ln p_i) \quad (5)$$

In this equation, the “2” was included in the denominator so that the total response, that is, the sum of the responses to parameter increase and parameter decrease, equals $\Delta y / \Delta \ln p_i$.

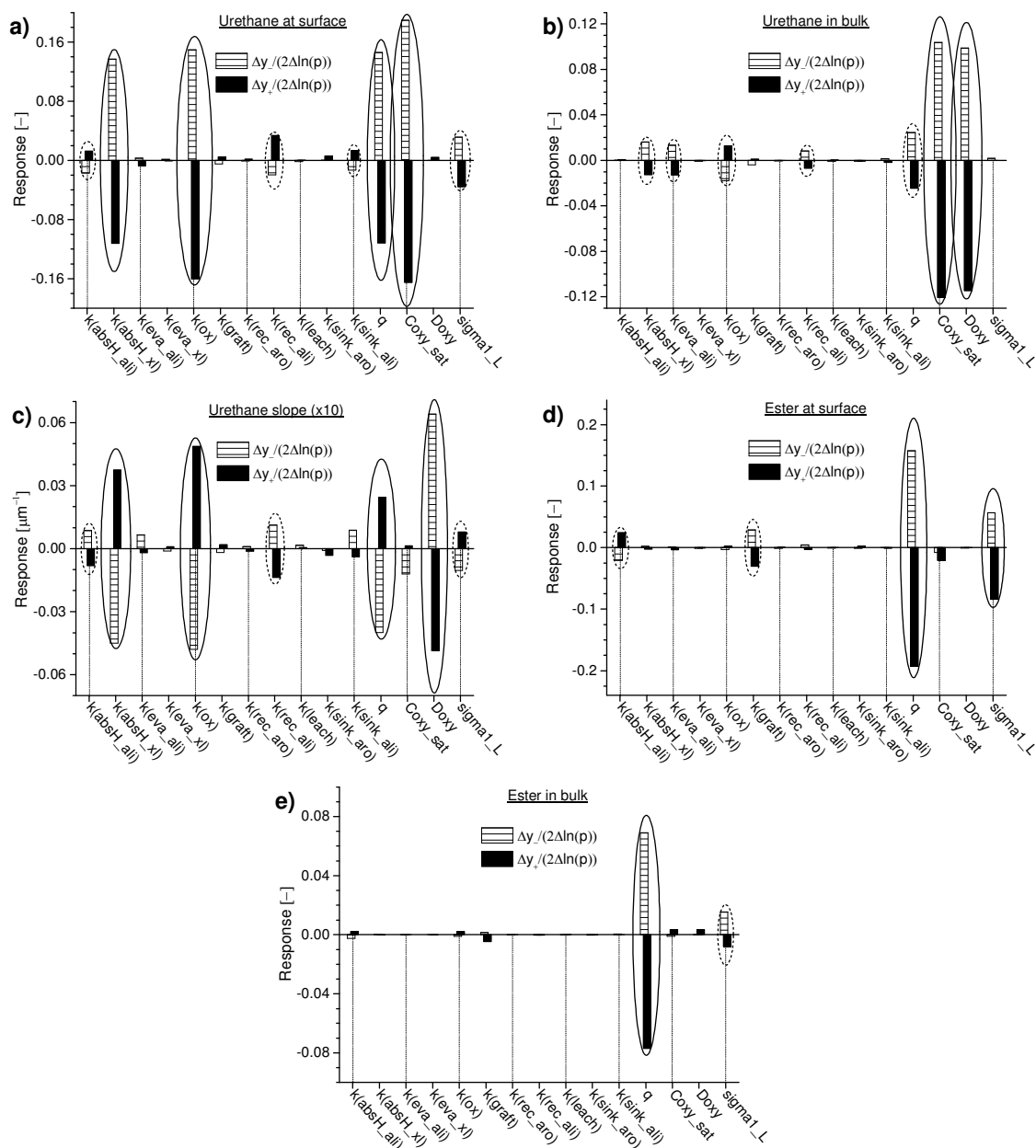


Fig. 8: Response plot for the parameter variation of a WOM exposure simulation for a thick coating including oxygen diffusion, with respect to the a) urethane bond surface fraction, b) urethane bond bulk fraction, c) urethane bond gradient slope (x10), d) ester bond surface fraction and e) ester bond bulk fraction. The ellipses shown indicate the high-influence (solid ellipses) and medium-influence (dashed ellipses) parameters for each observable. The dotted vertical lines are shown to guide the eye.

The parameter change was normalised on the change in the logarithm of p_i instead of the change in p_i itself, for the reason that the absolute values of the different p_i 's can differ a great deal (between first and second order rate constants for example). The logarithm of p_i then gives a better comparison for all these parameters together, since it leads to a shift by the

logarithm of the multiplication factor that does not depend on the magnitude of p_i itself ($\Delta \ln p_i = \ln f_i p_i - \ln p_i = \ln f_i$). The results of this sensitivity analysis are shown in Fig. 8.

When focussing on the most influential parameters for each observable (ellipses in the figure), some general remarks can be made. Reduction of the urethane bond fraction at the surface (Fig. 8a) is most sensitive to an increase in: the rate constant of hydrogen abstraction from a crosslinker arm, the rate constant of oxidation, the quantum efficiency and the oxygen saturation concentration. Since the increase of all these parameters leads to either higher concentrations of radicals on the NH-side of the urethane bond or to higher oxidation rates, this makes perfect sense.

By comparing the urethane bond surface fraction to the bulk (Fig. 8b), some interesting differences can be found. Next to the oxygen saturation concentration, the diffusion coefficient for oxygen has the largest influence. This is logical, because diffusion of oxygen plays a large role in regulating the oxygen concentration deeper inside the coating, whereas it does not influence this value at the very surface. Another important difference between Fig. 8a and Fig. 8b is that the influence of the oxidation rate constant has opposite signs, in other words, when the oxidation rate constant is increased, urethane bond breakage in the bulk is slowed down. The reason for this is that an increased oxidation rate throughout the coating, achieved by increasing k_{ox} , leads to a lower amount of oxygen inside the coating that is able to diffuse all the way through. The bulk becomes effectively depleted of oxygen and hence the oxidation rate slows down. In this way, the character of oxidation rate reactions in the bulk changes between reaction-limited and diffusion-limited.

The response of the steepness of the urethane bond gradient (Fig. 8c) looks rather complicated and also somewhat more asymmetric than the response for the other observables when comparing R_+ to R_- . This increased asymmetry is probably related to the fact that the urethane bond gradient slope is determined using a thicker slice of the box as compared to the

other observables (the data between -6 and -14 μm was used to fit a line, the slope of which determines this quantity).

The responses related to ester bond fractions (Fig. 8d and Fig. 8e) are most sensitive to parameters that can be directly related to photolysis rates and are rather insensitive to all oxidation-related parameters. Relevant parameters include the grafting rate constant and σ_{1,eff_L} (influencing absorptivity increase) and the scission quantum efficiency.

A careful comparison of all the subfigures from Fig. 8 together reveals that there are four rate constants that do not significantly influence the five observables that were studied. Indeed, when the simulation was performed again, but now with these four rate constants set to 0 and thus eliminating the corresponding mechanisms, the simulation outcome with respect to these five observables is unchanged. Please note that this does not mean that these four mechanisms do not influence the simulated degradation pathway at all - they do, but with respect to other observables than the five that were studied here, such as, for example, (gradients in the) radical concentration, oxidation state, fraction of new crosslink bonds and the remaining bead fraction. For this reason, these four rate constants ($k_{\text{eva_xl}}$, k_{leach} , $k_{\text{sink_aro}}$, $k_{\text{rec_aro}}$) were denoted as “secondary rate constants” in Table 4, as they are not of direct importance for the five observables studied, in contrast with the remaining seven rate constants that are of primary importance. The other physical parameters from Table 4 (σ_{1,eff_L} , q , D_{O_2} and $C_{\text{O}_2,\text{sat}}$) are of significant influence on the five studied observables as well.

3.6 Parameter optimisation and discussion

In the best case imaginable, the simulation result matches perfectly to the experimental data. This would imply that the defined degradation mechanisms and conditions have an excellent correspondence with reality and that the input parameters used have their “true” values. Even though this situation is highly unlikely, it is still useful to investigate how close this ideal can be approximated with the current reaction mechanisms and an optimised set of parameters

[P_{opt}]. In Supporting Information 3, a mathematical procedure is described to obtain [P_{opt}] using the results of the sensitivity analysis that was described in the previous section.

Looking at the values of the primary rate constants after optimisation, it can be seen that they are all of the same order of magnitude within their first and second order reaction classes. The rate constant for hydrogen abstraction turns out to be somewhat larger for the crosslinker arm bead (α -position to the NH of the urethane bond) as compared to the aliphatic bead (α -position to the ester bond), which is in line with the idea that the former hydrogen is more weakly bound than the latter¹⁸. The outcome for the other optimised physical parameters can be compared more quantitatively to knowledge that is available from experiments. The scission quantum efficiency ($0.75 \cdot 10^{-3}$) compares well to the value that can be derived from the kinetic model in the experimental reference ($0.95 \cdot 10^{-3}$), considering the ester bond surface degradation rate of 2.5% week⁻¹ as determined from infrared microscopy. The absorption cross-section σ_{1,eff_L} can be compared to its non-enhanced (monophenyl) value σ_{0,eff_L} to find that the predicted enhancement factor for photon absorption due to biphenyl formation equals 12. A comparison of this value to experimental data could not be made due to the lack of available UV-VIS data for suitable model compounds. The value of the oxygen diffusion coefficient ($1.2 \cdot 10^{-13} \text{ m}^2\text{s}^{-1}$) compares well to available literature data for polymers¹ and was also confirmed experimentally by oxygen permeation measurements on virgin and degraded free-standing films of WOM-exposed polyester-urethane, for which a constant value of about $3 \cdot 10^{-13} \text{ m}^2\text{s}^{-1}$ at room temperature was obtained. The value of the oxygen saturation concentration ($0.99 \text{ mol}\cdot\text{m}^{-3}$) from the simulation in air translates into an oxygen solubility $S = 0.12 \text{ cm}^3(\text{STP})\text{cm}^{-3}\text{bar}^{-1}$, which is also of the same order as literature values reported for other polymers¹⁹ and agrees well with oxygen permeation measurement results[†], which yielded a range of about $0.1\text{-}0.3 \text{ cm}^3(\text{STP})\text{cm}^{-3}\text{bar}^{-1}$ at room temperature.

[†] The details of these permeation measurements will be discussed in a future publication.

Even though the final simulation of coating degradation during WOM exposure gives a satisfactory description of the experimental data and the resulting parameter values seem realistic, there is always room for improvement. Especially the steepness of the urethane bond gradients (Fig. 7a) is not predicted very well by the simulation with $[P_{opt}]$. In fact, the simulation result can get much closer to the experimental slope if one changes a few parameter values, but in that case, the degradation rate for urethane bonds in the bulk becomes way too low and hence the overall match to experiment is not improved. By taking a careful look at Fig. 8b and Fig. 8c, this problem can be readily understood. The most efficient way to increase the slope without disturbing the urethane bond level at the surface, is by reducing the oxygen diffusion coefficient. However, the urethane bond level in the bulk is also very sensitive to this change and increases (that is, the degradation rate is decreased) for the reason that has been discussed before: oxygen depletion in the bulk. Indeed, if the stationary bulk oxygen concentration of this situation is compared to the situation resulting from $[P_{opt}]$, a reduction of 60% is found.

Improvement of the simulation outcome is thus related to further model improvement. The two depth dependencies that have been introduced so far, that is, photon absorption and oxygen concentration, are seemingly insufficient to rationalise the experimentally found urethane bond profiles. The effect of water cycling in the Weather-Ometer has not been taken into account explicitly, although it may be more logical to think about this factor in the context of lateral inhomogeneity than in the case of depth inhomogeneity, considering the short cycle times involved. Another factor seems to play a role here, but based on the available information, it would be mere speculation to propose its nature here.

4 Conclusions

A numerical method to simulate the photodegradation process of a polymer coating has been developed and has been applied to the degradation process that a urethane-crosslinked PNI

clearcoat undergoes during Weather-Ometer exposure. The simulation method is based on a kinetic Monte Carlo scheme and is able to simulate the space-resolved evolution of a macroscopic, three-dimensional volume of material during exposure. Several steps that are required to set up such a simulation have been outlined, such as coarse-graining of the molecular structure and the degradation chemistry, the definition of the main degradation mechanisms and the incorporation of the kinetics of these processes on different scales.

The input of the WOM-degradation simulations is largely based on quantitative experimental data that have been obtained earlier¹². With respect to modelling the absorption of UV photons, for example, the wavelength dependence of this process was modelled by defining two wavelength regimes based on the penetration depth of photons into the coating, that is, a regime of short wavelength photons (< 294 nm) that penetrate only a few micrometres and a long wavelength regime (> 294 nm) of photons that penetrate all the way through a typical clearcoat with a 40 micrometre thickness.

Three different simulations with a constant (optimised) set of input parameters have been performed and analysed. These simulations were used to verify the simulation method by comparing the outcome to experimental results and to obtain a more detailed insight into the degradation process.

The first simulation was that of a thin coating, thickness 4 μm , which is representative of coating samples for FTIR and UV-VIS transmission spectroscopy measurements in the experimental reference. The evolution of the optical absorbance and the urethane bond fraction could be matched well with the experimental data. For the ester bond fraction, the simulation resulted into the correct rate of scission and followed the experimental data set after correcting for the constant offset that originates from the initial phase of the degradation experiment.

The second and third simulations were those of a thick coating, thickness 40 μm , which is

representative for a typical clearcoat such as those used for infrared microscopy measurements in the experimental reference. The second simulation, without consideration of oxygen diffusion, matched well with the experimental data for the (shifted) ester bond concentration, which indicates that the modelling of photon absorption and ester bond scission as done here yields a realistic description of depth-resolved photolysis. For the urethane bond concentration, however, only the surface value was well matched. The predictions of the bulk concentration and the slope of the urethane bond gradient were much improved after the incorporation of oxygen diffusion into the simulation scheme, which was done for the third simulation. The local concentration of oxygen plays an important role in the depth-inhomogeneity of oxidation reactions and was found to stabilise during intermediate exposure times, at values dependent on the oxygen diffusion coefficient and the oxygen saturation concentration.

A sensitivity analysis of all simulation parameters with respect to five resulting observables, for which also the experimental values have been determined, has shown that different observables are sensitive to different parameters (and thus associated reaction mechanisms). The simulated ester bond concentration is mainly sensitive to parameters that can be directly related to photolysis rates and photon absorption, whereas the urethane bond concentration is most sensitive to hydrogen abstraction rates in the α -position to the NH of the urethane bond, oxidation rates, the oxygen saturation concentration and, if not too close to the surface, to the oxygen diffusion coefficient. The latter parameter provides a coupling between the bulk level and the slope of the urethane bond gradient. The scission quantum efficiency significantly influences every observable as it regulates the overall time scale in the degradation simulations. For four of the incorporated mechanisms, it was found that their influence on the five observables was negligibly small, resulting in a final simulation scheme with 8 essential reaction mechanisms and 11 associated variable parameters.

Based on the result of the sensitivity analysis, a numerical optimisation procedure has been used to determine the optimised set of input parameters that was used for the three aforementioned simulations. The resulting values of physical parameters such as the scission quantum efficiency, the diffusion coefficient for oxygen and the oxygen saturation concentration, were found to show good agreement with experimental data for this polyester-urethane and literature data for comparable materials.

Although the match of the final (third) simulation to experimentally measured concentration gradients is satisfactory, there is still room for improvement of the simulated urethane bond concentration. This improvement should be sought in extending the list of simulation mechanisms that has been presented here. Apparently, incorporation of another factor besides photon absorption and oxygen diffusion is required for a complete description of depth inhomogeneity for the breakage of urethane bonds.

5 Acknowledgements

This research forms part of the research programme of the Dutch Polymer Institute (DPI), project #713. Special thanks are given to dr. Mat Celina (Sandia National Laboratories, Albuquerque, U.S.A.) for performing the oxygen permeation measurements.

6 References

- [1] Rabek JF. Polymer photodegradation - mechanisms and experimental methods. 1st ed. London: Chapman and Hall; 1995.
- [2] White JR, Turnbull A. Weathering of polymers: mechanisms of degradation and stabilization, testing strategies and modelling. *Journal of Materials Science*. 1994;29:584-613.
- [3] Martin JW. A Stochastic Model for Predicting the Service Life of Photolytically Degraded Poly(methyl Methacrylate) Films. *Journal of Applied Polymer Science*.

- 1984;29:777-94.
- [4] Hunt FY, Galler MA, Martin JW. Microstructure of Weathered Paint and Its Relation to Gloss Loss: Computer Simulation and Modeling. *Journal of Coatings Technology*. 1998;70:45-53.
- [5] Hinderliter B, Croll SG. Monte Carlo Approach to Estimating the Photodegradation of Polymer Coatings. *JCT Research*. 2005;2:483-91.
- [6] Croll SG, Hinderliter BR, Liu S. Statistical approaches for predicting weathering degradation and service life. *Progress in Organic Coatings*. 2006;55:75-87.
- [7] Hinderliter BR, Croll SG. Simulations of Nanoscale and Macroscopic Property Changes on Coatings with Weathering. *JCT Research*. 2006;3:203-12.
- [8] Kiil S. Model-based analysis of photoinitiated coating degradation under artificial exposure conditions. *Journal of Coatings Technology and Research*. 2012;9:375-98.
- [9] Bauer DR. Predicting In-Service Weatherability of Automotive Coatings: A New Approach. *Journal of Coatings Technology*. 1997;69:85-96.
- [10] Nichols ME, Frey JF. Statistical modeling of coating lifetimes in disparate environments. *Journal of Coatings Technology and Research*. 2015;12:49-61.
- [11] Kiil S. Mathematical modeling of photoinitiated coating degradation: Effects of coating glass transition temperature and light stabilizers. *Progress in Organic Coatings*. 2013;76:1730-7.
- [12] Adema KNS, Makki H, Peters EAJF, Laven J, van der Ven LGJ, van Benthem RATM, de With G. Depth-resolved infrared microscopy and UV-VIS spectroscopy analysis of an artificially degraded polyester-urethane clearcoat. *Polymer Degradation and Stability*. 2014;110:422-34.
- [13] Makki H, Adema KNS, Peters EAJF, Laven J, van der Ven LGJ, van Benthem RATM, de With G. A simulation approach to study photo-degradation processes of polymeric

- coatings. *Polymer Degradation and Stability*. 2014;105:68-79.
- [14] Rossi G, Monticelli L, Puisto SR, Vattulainen I, Ala-Nissila T. Coarse-graining polymers with the MARTINI force-field: polystyrene as a benchmark case. *Soft Matter*. 2011;7:698.
- [15] Rossi G, Giannakopoulos I, Monticelli L, Rostedt NKJ, Puisto SR, Lowe C, Taylor AC, Vattulainen I, Ala-Nissila T. A MARTINI Coarse-Grained Model of a Thermoset Polyester Coating. *Macromolecules*. 2011;44:6198-208.
- [16] Malanowski P, Huijser S, Scaltro F, van Benthem RATM, van der Ven LGJ, Laven J, de With G. Molecular mechanism of photolysis and photooxidation of poly(neopentyl isophthalate). *Polymer*. 2009;50:1358-68.
- [17] Malanowski P, van Benthem RATM, van der Ven LGJ, Laven J, Kisin S, de With G. Photo-degradation of poly(neopentyl isophthalate). Part II: Mechanism of cross-linking. *Polymer Degradation and Stability*. 2011;96:1141-8.
- [18] Wilhelm C, Gardette J-L. Infrared analysis of the photochemical behaviour of segmented polyurethanes. 1. Aliphatic poly(ester-urethane). *Polymer*. 1997;38:4019-31.
- [19] Van Krevelen DW. *Properties of Polymers, Their Estimation and Correlation with Chemical Structure*. 2nd rev. ed. ed. Amsterdam: Elsevier; 1976.
- [20] Matsumoto M, Nishimura T. Mersenne Twister: A 623-Dimensionally Equidistributed Uniform Pseudo-Random Number Generator. *ACM Transactions on Modeling and Computer Simulation*. 1998;8:3-30.
- [21] Erich SJF, Laven J, Pel L, Huinink HP, Kopinga K. NMR depth profiling of drying alkyd coatings with different catalysts. *Progr. Org. Coat.* 2006;55:105-111.
- [22] Laven J, Aravind, UK and van der Linde R. The Chemical Drying Process in Alkyd Emulsion Paint Films. Proc. 29th Int. Conf. Coatings Sci. Technol. Greece, Athens. 2003;201-218.